Registration, lesion detection, and discrimination for breast dynamic contrast-enhanced magnetic resonance imaging

Chapter x

Registration, Lesion Detection and Discrimination for Breast Dynamic Contrast Enhanced Magnetic Resonance Imaging

1.1 Introduction

Breast cancer is the second most common malignancy after lung cancer and the most common cancer in women[1,2].

Dynamic contrast-enhanced (DCE) breast MRI, in which the breast is imaged before (unenhanced image), during and after (enhanced images) the administration of a contrast agent, provides a noninvasive assessment of the microcirculatory characteristics of tissues in addition to traditional anatomical structure information[3].

DCE-MRI shows promise in detecting both invasive and ductal carcinoma in situ cancers, gives information on the biological aggressiveness of tumors, may be used to evaluate response to neoadjuvant chemotherapy[4–7] and is therefore increasingly used in breast cancer diagnosis as an adjunct to conventional imaging techniques[8,9]. Furthermore, DCE-MRI is highly sensitive, allowing detection of malignancy that is occult on physical examination, mammography, and sonography. However, despite its high sensitivity, several factors have precluded more widespread use of this technique. Current challenges include the lack of standardized acquisition protocols, time required for image processing and interpretation, and variable specificity of this imaging tool. In addition, the particular combinations of morphologic and kinetic features that best discriminate benign from malignant lesions have yet to be fully defined[10].

In the last years, Computer-aided diagnosis (CAD) systems have been introduced to overcome these obstacles. CAD systems aid in the visualization of kinetic information by providing color mapping, facilitate analysis through graphical and quantitative representations and provide an index of suspicion. In

order to compute morphological features and kinetic curves for use in predicting pathology probability (discrimination step), a typical CAD system also includes a procedure of motion compensation between unenhanced and enhanced images (registration) and a procedure of lesion identification (lesion detection).

In this chapter a specific approach is chosen and described for each step of a CAD system (CADBREAST MRI, research version, im3D).

1.2 Registration

This step is aimed at correcting possible misalignment in the dynamic sequence due to patient motion. It was performed by registering all the contrast-enhanced images with reference to the unenhanced sequence.

1.2.1 Method

The registration method, illustrated in Fig x.1, is based on the method proposed by Rueckert[11], and was implemented using the insight toolkit (itk)[12].

To reduce the computational burden, the registration was performed at a minimal predefined resolution in each axis direction. Therefore, if the frames of the dynamic series presented a lower resolution in any of the directions, the images were down-sampled to the predefined minimal resolution. Otherwise, registration was performed at original resolution. In addition, the registration was performed within a rectangular region of interest, containing the relevant part of the scans for the diagnosis (i.e., breasts and axillae), which was automatically

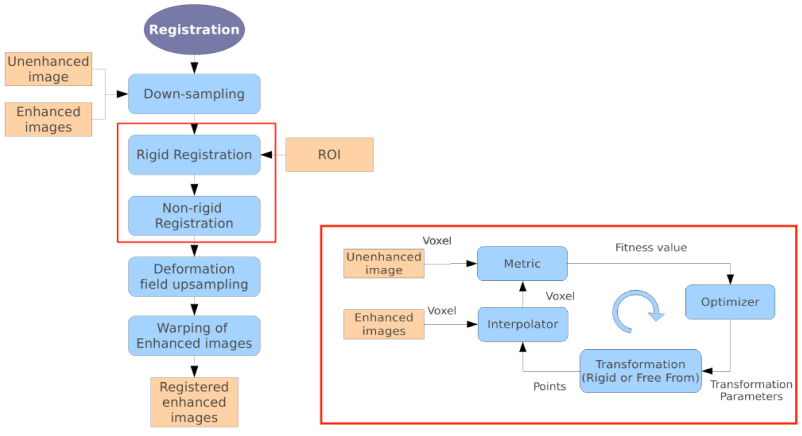

Figure x.1. (a) Scheme of the registration method. (b) Basic components of the itk registration framework used for the rigid and non-rigid registration steps.

determined based on the maximum and minimum points of the breast (as defined in section 1.3.1).

The registration itself consists of two main steps. First, the global misalignment was compensated by using a translation and a rigid-body transformation. Subsequently, local motion was corrected by a free-form deformation model based on B-splines[11]. In all cases, mutual information was used as image similarity measure, in particular by the method specified by Mattes et al[13]. Optimization was carried out by means of a gradient descent optimizer for the rigid registrations, and of the LBFGSB (Limited memory - Broyden, Fletcher, Goldfarb, and Shannon - for Bound constrained optimization) optimizer for the nonrigid sub-step[14]. If the contrast-enhanced frames were down-sampled before the registration, the respective deformation fields were up-sampled to the original resolution. Finally, the original contrast-enhanced frames were warped to obtain the transformed (aligned) contrast-enhanced frames by applying the respective deformation field. In the warping, B-spline interpolation was used to minimize the introduction of sampling artifacts.

1.2.1 Results

The registration method was tested on 24 patients (mean age 55 years, range 37-79 years) acquired on a 1.5T scanner using a 3D axial FLASH sequence[15–16]. Sixteen of 24 patients were randomly selected while the remaining 8 were added as they presented relevant artifacts due to patient movement.

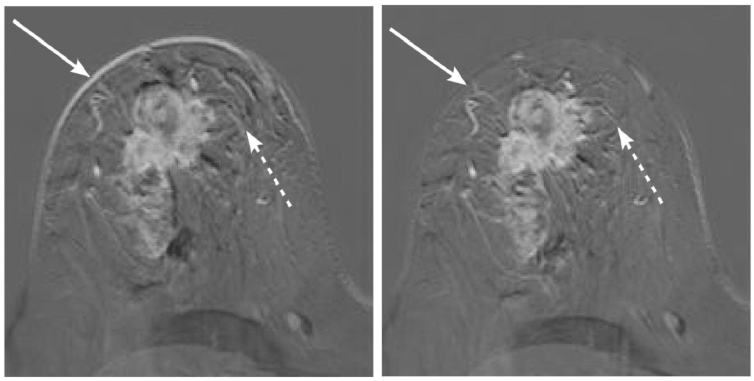

(a) (b)

Figure x.2 Comparison between subtracted images with and without registration. (a) Subtraction artifacts due to patient movement are visible along the breast profile (plain arrow), in the breast parenchyma (dot arrow), at lesion and vessel borders, as well as at the borders of fat lobules. These artifacts may introduce spurious enhancing voxels, thus increasing the number of FP findings at segmentation. (b) Subtraction artifacts are dramatically reduced when elastic registration is used.

The registration method was applied to the enhanced sequences with reference to the unenhanced one. Registered (REG) and non-registered (N-REG) axial images and maximum intensity projections (MIPs) of the first enhanced subtracted frame were randomized and blindly evaluated by two radiologists separately by scrolling the axial images and rotating the MIPs, with free windowing. Image quality was assessed for both axial images and MIPs. Readers were asked to define equivalence or superiority of one of the two datasets of each patient, simultaneously presented. Finally, the im3D CADBREAST MRI system (research version) identified suspicious enhancements (prompts) for REG and N-REG images. A radiologists excluded prompts related to real findings; the remaining false prompts and their volume were obtained for both REG and N-REG images. Sign test, weighted kappa (k), and Wilcoxon exact test were used[17].

Image quality of REG-MIPs was found to be significantly superior than that of N-REG-MIPs for both readers (p-value<0.001) with a quite good inter-rater agreement (k=0.5). Image quality of REG-axial images was found to be slightly better than that of N-REG axial images by both readers without significant difference. The mean number of false prompts per patient was 29.4±17.7 on N-REG and 25.0±16.5 for REG (p-value=0.041). Excluding one patient with wrong segmentation of the heart, the mean volume of false prompts was 13,000±11,641 mm^3 for N-REG and only 4,345±4,274 mm^3 for REG (p-value<0.001).

Examples of how registration was able to compensate for motion artifacts are shown in Fig. x.2 and Fig. x.3.

1.3 Lesion detection

As DCE-MRI data analysis is time-consuming, lesions may be isolated by segmentation to reduce reporting time.

This image processing procedure is preliminary to the extraction of quantitative information on lesion morphology, kinetics and volume, and to distinguish viable from non-viable tissue[18]. Most segmentation methods are manual or semi-automatic, and therefore may be affected by high inter- and intra-observer variability[19–21]. On the contrary, a fully automatic lesion segmentation process has the potential to reduce reading time and provide more reproducible results. Unfortunately, few papers have addressed automatic lesion detection and segmentation techniques for breast DCE-MRI[22–24]. Furthermore, to our knowledge these methods have been tested only on non fat-saturated (fat-sat) contrast-enhanced images. Fat-saturation allows to enhance the contrast between lesion and surrounding tissue[6], but introduces additional challenges for lesion segmentation, such as artifacts from inhomogeneous signal saturation and a lower contrast-to-noise-ratio between enhanced lesions and surrounding parenchyma[25].

A new, fully automatic algorithm for breast lesion detection is presented[26]. The method has been conceived to run on both fat-sat and non-fat-sat DCE-MRI datasets obtained from different MR scanners.

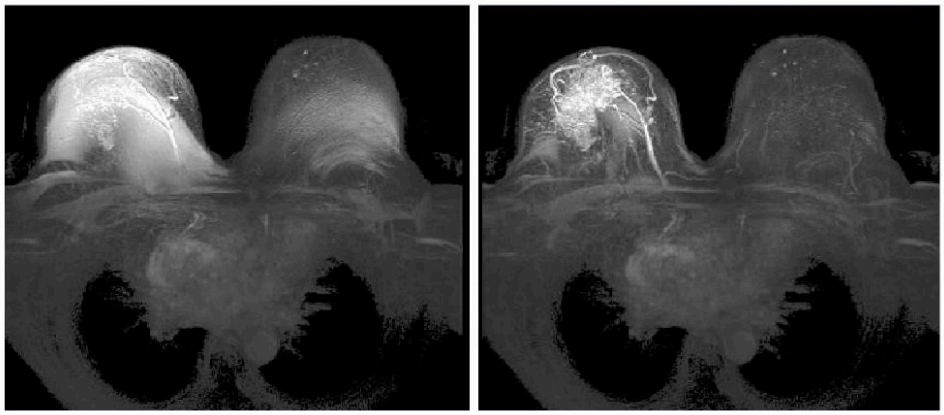

(a) (b)

Figure x.3 Comparison of non-registered (a) and registered (b) MIPs. The image quality is significantly superior in registered images (in N-REG images the motion artifacts introduce spurious enhancing voxels).

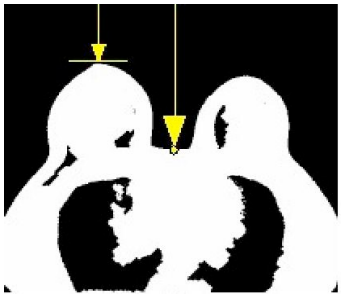

Figure x.4. Arrows point to the maximum and minimum points.

1.3.1 Method

The detection pipeline (CADBREAST MRI, research version, im3D) consists of four main processing steps, none of which requires user interaction:

(1) breast segmentation, to automatically identify the breast and axillary regions;

(2) lesion detection, to extract suspicious contrast enhanced areas;
(3) false positive (FP) reduction, to identify and discard regions incorrectly extracted.

Breast segmentation

The breast segmentation itself is preceded by a process of identification of the approximate size and location.

A rough estimate of breast location was obtained by identifying the maximum point, defined as the most anterior point reached by the breasts, and the minimum point, which is the deepest point within the concavity between the breasts (Fig. x.4).

These measures were obtained following a rough segmentation of the patient's body, based on Otsu's thresholding algorithm[27]. The central line, defined as the line running along the concavity between the breasts, was computed by exploiting image symmetry and by searching for the skin voxel around the center of each slice.

Once the central line has been obtained two different procedure for breasts segmentation were performed. If fat-sat is not used, the breasts can be easily identified based on the high signal intensity of fat tissue. Similarly to the technique used by Twellmann et al.[24], a satisfactory segmentation can be obtained by combining morphological operations and Otsu's thresholding. On the contrary, if fat-sat is used, intensity alone is not sufficient to obtain a reliable segmentation. In this case, an a priori knowledge of the main anatomical

structures in the field of view was exploited, using an atlas-based segmentation scheme. A simplified atlas was used in which the breasts, heart, chest wall and lungs have been previously manually segmented and color-coded. Because breast size and shape may vary considerably across subjects, three different atlases were generated for large, medium and small breasts. The most appropriate model was automatically selected for each patient according to breast size, measured as the distance between the maximum point, and the minimum point along the central line.

The patient body was identified by the above mentioned Otsu's thresholding method, the image was down-sampled to a predefined resolution to reduce the computational burden, and then registered to the appropriate breast atlas.

Two examples of breasts segmentation results are shown in Fig. x.5.

The two methodologies yield slightly different results in the axillary area, but this is not compromising for the lesion detection. Axillae, supraclavicular fossae, chest wall, and anterior mediastinum can be assessed by breast MRI (e.g. to search for enlarged lymph nodes) but their evaluation could be omitted as there is no evidence of its diagnostic value[25].

Lesion detection

Differences in vascular permeability[28,29] and other technical and physiological parameters, including type and dose of contrast material[30,31], cause large physiologic variations in the contrast enhancement of breast lesions. Differences may depend on lesion histology, on the timing of imaging or on inhomogeneities within the lesions, such as those observed in necrotic areas or in fibrosis. The proposed approach used the subtracted mean intensity projection image over time (mIPT) in order to consider the nonuniform uptake of contrast, reducing at the

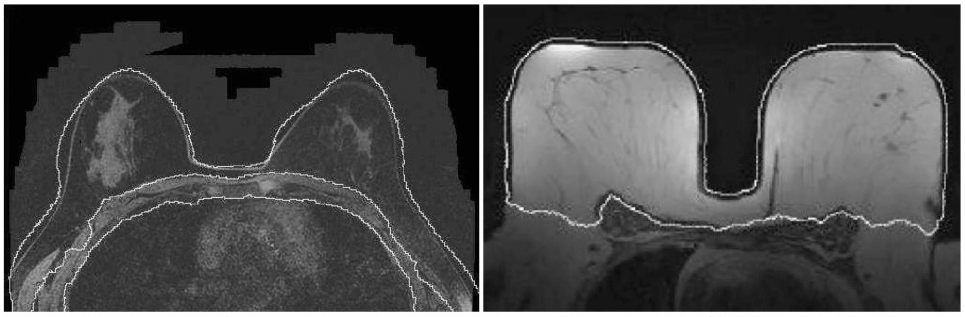

a) b)

Figure x.5. (a) Example of breast segmentation for a study acquired with fat-saturation. The breast mask extends further than in non-fat-sat sequences, as defined by the breast atlas. (b) Example of breast segmentation for a study acquired without fat-saturation.

same time the computational burden associated with the processing of all the contrast-enhanced registered frames. Being the dynamic sequence a 4D image ($x \times y \times z \times t$), where t is time, the mIPT is the 3D image ($x \times y \times z$) formed by averaging along t axis each voxel of each registered enhanced frames. In order to neglect the contribution of regions which do not show contrast enhancement, subtraction of the unenhanced frame was performed.

Different scanners, coils, acquisition modalities, types and amounts of contrast agent injected, patients' physiology, and other external factors, result in significant variations of image intensities among images acquired in different hospitals, in different patients, or even among different examinations from the same patient[30,31]. The subtracted mIPT was normalized by contrast enhancement of the mammary vessels to compensate for these effects.

In the first dynamic phase images it is possible to obtain the best "angiographic effect" for both arteries and veins, because in the subsequent acquisitions a more pronounced distribution of contrast material in the interstitial space reduces the vascular enhancement[32]. Therefore, the mammary vessels were automatically segmented on the first subtracted contrast-enhanced frame. Referring to the position of the central line, a suitable ROI was automatically selected by placing a rectangle of a fixed size in each slice. The mammary vessels were then identified by applying to the ROI the multiscale 3D Sato's vessel enhancement filter, which is based on the eigenvalues of the Hessian matrix[33,34].

The Sato's vessel enhancement filter considers the mutual magnitude of the eigenvalues as indicative of the shape of the underlying object: isotropic structures are associated with eigenvalues which have a similar nonzero magnitude, while vessels present one negligible and two similar nonzero eigenvalues. Let the eigenvalues of the Hessian matrix be λ_1, λ_2, λ_3 (with $\lambda_1>\lambda_2>\lambda_3$). On a given scale, vesselness is thus defined as:

$$V_\sigma = \begin{cases} \exp\left(-\frac{\lambda_1^2}{2(\alpha_1\lambda_c)^2}\right) & \lambda_1 \le 0, \lambda_c \ne 0 \\ \exp\left(-\frac{\lambda_1^2}{2(\alpha_2\lambda_c)^2}\right) & \lambda_1 > 0, \lambda_c \ne 0 \\ 0 & \lambda_c = 0 \end{cases} ; \qquad \text{(x.1)}$$

where $\lambda_c = \min(\lambda_2, \lambda_3)$, α_1 and α_2 were set to 0.5. The σ footer in V_σ indicates that the vesselness is computed on a smoothed version of the image and is therefore representative of the variations of image intensity on the σ spatial scale. As vessels in the breasts could have different diameters, the vesselness is evaluated on a range of spatial scales, and the highest response is selected for each voxel. Specifically, the vesselness response is computed at 6 exponentially

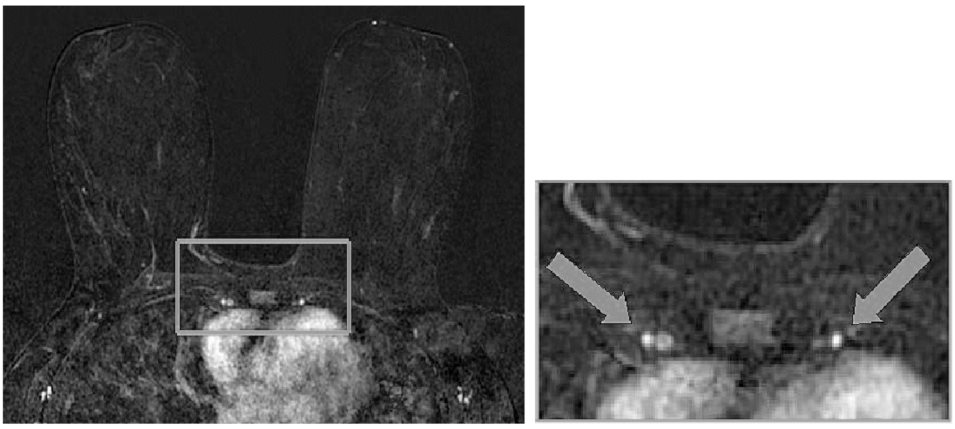

(a) (b)

Figure x.6 (a) First subtracted contrast-enhanced frame with the region where the mammary vessels are located in the rectangle. (b) Zoom of the region in the rectangle highlighted in (a). Arrows point mammary arteries that will be segmented by the system.

distributed scales between the maximum and minimum scales $\sigma_{min} = 0.5$ and $\sigma_{max} = 1.0$.

A threshold, equal to half the maximum vesselness value observed in the ROI identified as described above, was then applied to select the most vessel-like voxels. Figure x.5 shows an example of mammary vessels.

The mean contrast enhancement of the mammary vessel voxels in the first contrast-enhanced frame was considered as normalization factor.

After normalizing the subtracted mean intensity projection, regions showing contrast enhancement were extracted. Even if the contrast-enhanced frames were normalized, a fixed threshold was not found to be suitable to successfully segment lesions on all scans. As a consequence, a global threshold T_I was empirically determined as:

$$T_I = mean_I + \frac{max_I}{3} \qquad \text{(x.2)}$$

where $mean_I$ is the mean value of the normalized intensity histogram of the breast and axillary region and max_I is the highest intensity value observed in the same region.

Lesions and connected feeding vessels are often segmented together, leading to lesion oversegmentation, which could reduce the diagnostic quality of the segmentation and limit the performance of segmentation-based CAD applications. To avoid this risk, the eigenvalues of the covariance matrix were

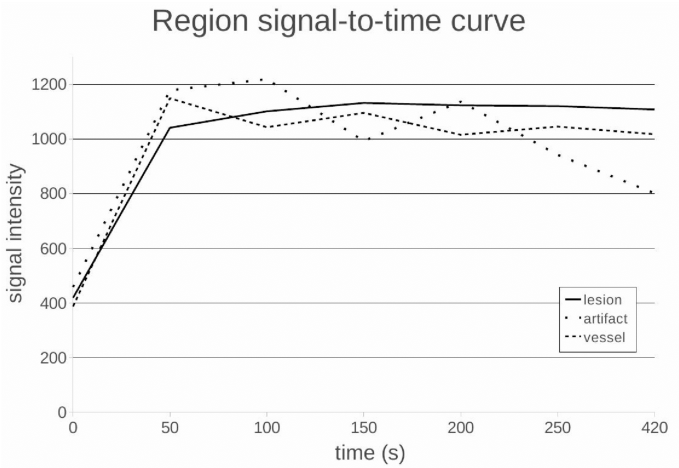

Figure x.6. Signal intensity curves calculated over an entire connected component in the case of a lesion, a vessel and an artifact.

extracted for each voxel, and the ratio between the highest and medium eigenvalues was used as a vesselness measure. Voxels with a ratio larger than a fixed threshold T_v were labeled as vessels and excluded from lesion detection. Connected components were then extracted from the resulting mask.

FP reduction

The method based on the covariance matrix eigenvalues, above described, do not completely discard all vessels,therefore, together with motion artifacts and noise, they contribute to the number of FP.

A few heuristic criteria were applied in our algorithm to exclude regions showing contrast enhancement, different from lesions. First, regions with a volume of less than 20 mm^3 were excluded. Taking into account image resolution and possible lesion undersegmentation, this roughly corresponded to a lesion of 5 mm in diameter, which is the cutoff between foci and lesions[35].

Contrast enhancement kinetics can be classified as curves I, II and III with an increasing probability of malignancy (6%, 64%, and 87%, respectively)[36]. However, these curves are commonly referred to individual voxels or to a set of few contiguous voxels within a plane belonging to a single part of tissue with uniform vascular characteristics, and thus homogeneous contrast enhancement, whereas the average intensity curve calculated over an entire lesion (typically without homogeneous vascular characteristics) is generally more similar to the average signal intensity curves shown in Fig. x.6. Thus, the aim was to identify trends which are indicative of structures other than benign and malignant lesions, such as noise, artifacts or vessels. Empirically, some simple kinetic features were

found to identify trends rather typical of vessels or artifacts, as shown in Fig. x.6. For instance, artifacts due to noise and patient motion are usually characterized by high signal variations; hence, regions with standard deviation greater than a specific value, or with a higher-than-10% decrease or increase in signal intensity in the last frame, with respect to the second-last frame, were discarded. Furthermore, regions with mean intensity decreasing from the first to the second enhanced frame were discarded, as this pattern is found in vessels but not in lesions.

1.3.2 Results

Subjects and MRI Protocol

Algorithm performance was evaluated on a dataset of 48 DCE-MRI studies (mean patient age 51 years, range 31-79 years) performed on women with suspicion of breast cancer based on conventional imaging[26].

Nineteen (group A) of the 48 studies were acquired on a 1.5 T scanner, using a fat-sat 3D axial fast spoiled gradient-echo sequence and administering Gadopentetate dimeglumine, for a total of seven scans for each study (one baseline, 5 contrast-enhanced frames with 50-s time resolution, and one delayed frame acquired 7 minutes after contrast injection).

The remaining 29 studies (group B) were acquired on a different 1.5T scanner, using a dynamic 3D axial spoiled fast low angle shot sequence and administering Gd-BOPTA, for a total of six scans for each study (one baseline, 5 contrast enhanced frames taken 118 s apart). Fat-sat sequences were not performed in group B patients.

The whole dataset included 12 benign and 53 malignant lesions. The median of the largest diameter of benign and malignant lesions was, respectively, 6 mm (range, 5–15 mm) and 26 mm (range, 5–75 mm). Overall, there were 16 lesions sized 10 mm or less, 15 lesions between 11 and 20 mm, and 34 lesions sized larger than 20 mm.

Statistical analysis

A radiologist with more than 4 years of experience in breast MRI labeled a finding as a true positive if the lesion was confirmed at histology or at follow-up, otherwise it was defined as a FP.

Detection rate was calculated as the number of true positives (both malignant and benign) over the total number of lesions as defined at the reference standard, whereas sensitivity was calculated as the number of malignant lesions detected by the system over the total number of malignant lesions.

Lesions were grouped according to size (see Table x.1) and detection rate and sensitivity were calculated for each group. Sensitivity and detection rate values are presented with 95% confidence intervals (CIs) using the Wilson

method for single proportions. Detection rate and sensitivity were also separately calculated for fat-sat and non-fat-sat exams, and the χ^2 test was used to assess differences between the two subgroups.

The detection rate was analyzed separately for lesions satellite to index cancers detected by radiologists, for which a lesion-by-lesion pathological analysis was not reported.

FP findings were recognized by the radiologist according to the position (mammary or extra-mammary) and the type (vessels, image artifacts, lymph nodes, normal gland or other findings). The FP median, 1st and 3rd quartiles were calculated for the entire testing set, for the fat-sat and non-fat-sat subgroups.A two-sided Kruskal Wallis test was applied to test for differences between the medians for the total number of FP/patient. A p-value lower than 0.05 was considered statistically significant.

Results

The automatic algorithm detected 58 of the 65 lesions (89% detection rate; 95% CI 79–95%), including 52 of the 53 malignant lesions (98% sensitivity; 95% CI 90–99%). Detection rate and sensitivity according to lesion size are shown in Table x.1.

In the fat-sat subgroup, 20 of the 25 lesions (80% detection rate; 95% CI 61–91%) were detected, including 19 of the 20 malignant lesions (95% sensitivity; 95% CI 76–99%). In the non-fat-sat subgroup, 38 of the 40 lesions (95% detection rate; 95% CI 84–99%) were detected, including all 33 malignant lesions (100% sensitivity; 95% CI 90–100%). Differences in sensitivity and detection rate between the two groups were not statistically significant (p-value = 0.798 and p-value = 0.137, respectively).

Table x.1. Number of lesions and performance for each dimension group. Lesions were grouped according to the National Cancer Institute. Detection rate and sensitivity were calculated with a 95% confidence interval.

Lesions Dimension (mm)	# Malignant	# Benign	# Total	Detection Rate (Upper–Lower Limits; 95% CI)	Sensitivity (Upper – Lower Limits; 95% CI)
5-10	6	10	16	69% (44% - 86%)	100% (61% - 100%)
11-20	13	2	15	87% (62% - 96%)	92% (67% -99%)
> 20	34	0	34	100% (90% - 100%)	100% (90% - 100%)
Total	**53**	**12**	**65**	**89%(79% - 95%)**	**98% (90% - 99%)**

A total of 7 lesions with an average size of 7±3 mm (mean±SD) were missed by the algorithm, including 6 benign and 1 malignant nodules. Five of the undetected lesions were in dataset A including: 2 fibroadenomas, 2 small enhancements with a negative MRI follow-up of 5 and a 7 mm in size, respectively, and a 12-mm invasive ductal carcinoma. Missed lesions in dataset B were two 5 mm small enhancements unchanged at MRI follow-up. Examples of lesions detected and missed by the system are shown in Fig x.7.

In addition to malignant lesions histologically confirmed as a result of a lesion-by-lesion analysis in the pathological report, 17 lesions satellite to

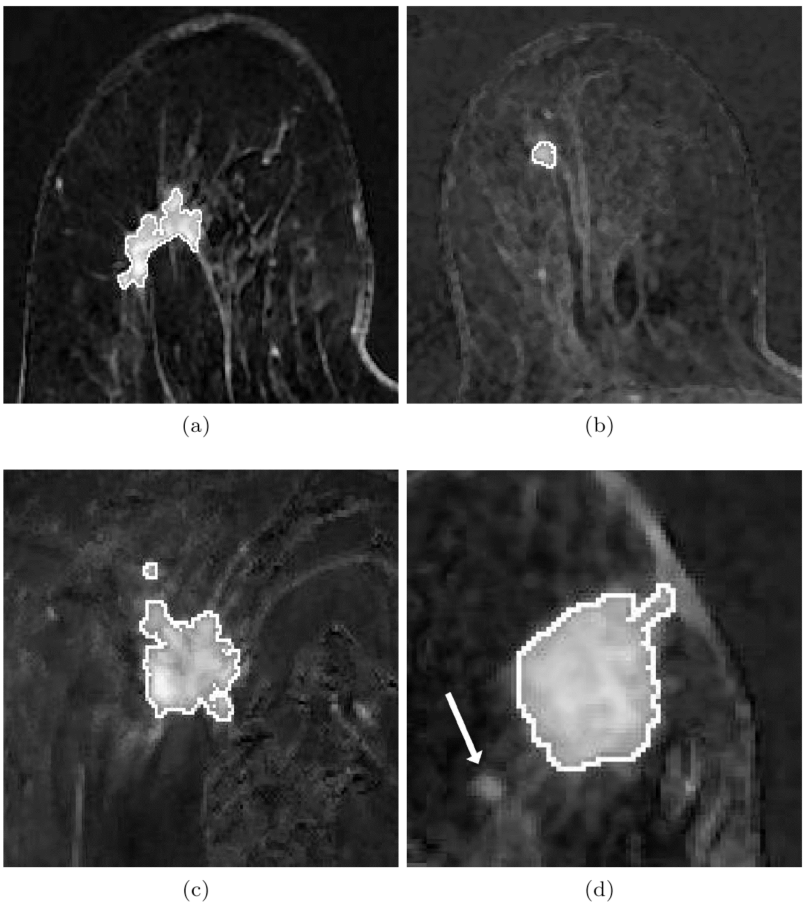

Figure x.7. Examples of segmentation results, superimposed on the normalized and subtracted mean projection over time. a: A 33-mm invasive ductal carcinoma (fat-sat image) correctly segmented; (b) a 7-mm invasive ductal carcinoma (fat-sat image) correctly segmented; (c) a 26-mm invasive ductal carcinoma (non-fat-sat image) correctly segmented; (d) a 25-mm invasive ductal carcinoma (fat-sat image) correctly segmented; here a 5-mm satellite lesion (arrow) was missed by the system.

malignant index lesions, with a median diameter of 7 mm (range, 5–20 mm) were detected by two radiologists. Sixteen of them (94%) were detected by the system.

Median mammary FPs per breast were 4 (1st–3rd quartiles 3–7.25), while median extra-mammary FPs per study were 2 (1st–3rd quartiles 1–5). Table x.2 shows the distribution of FP findings according to the type. For the fat-sat subgroup, median mammary FPs per breast were 4 (1st–3rd quartiles 2–7.25); median extra-mammary FPs per study were also 4 (1st–3rd quartiles 3–6). In the non-fat-sat group, median mammary FPs per breast were 4.5 (1st–3rd quartiles 3.5–7), while median extra-mammary FPs per study were 1 (1st–3rd quartiles 1–2). No statistical significant differences were detected between the two subgroups (p-value= 0.72).

Table x.2. Classification of FP findings according to the type

FP findings		
Type	**#**	**%**
vessels	267	54
artifacts *	113	23
gland	80	16
lymph nodes	2	0,4
other **	32	6

* i.e. chemical shift, skin, patient movements.

** i.e. nipple, pectoral muscle.

1.4 Lesion Discrimination

Lesion discrimination is a diagnostic stage in the CAD pipeline dedicated to recognize the level of malignancy of previously detected lesions.

Breast DCE-MRI allows to depict differences between malignant and benign lesions according to morphological and contrast-enhancement kinetics features of lesions.

Morphological attributes such as irregular or spiculated margins, irregular shapes, heterogeneous and peripheral internal contrast enhancement are important indicators of malignancy[37]. Signal-to-time curves with rapid decreasing of signal intensity after peak enhancement, reached approximately 2 or 3 minutes after contrast injection, are more frequently found in malignant lesions, whereas benign lesions have typically slow persistent enhancement increase[37].

Figure x.8 shows an example of a malignant lesion with irregular margins and heterogeneous internal enhancement and a benign lesion with regular margins and homogeneous internal enhancement.

Clinical interpretation of the kinetic and morphological properties is subjective and qualitative, therefore several studies have proposed computer assisted approaches.

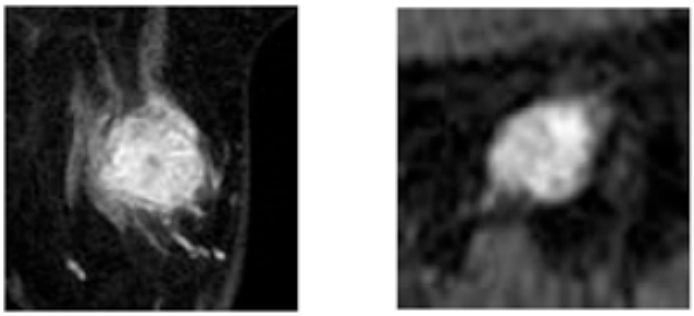

Figure 1 Examples of invasive ductal carcinoma (left) and benign fobroadenoma (right) breast lesions.

Gihuijs et al.[38,39] extracted morphological and kinetic features from lesions segmented manually or semi-automatically after manual indication of a seed point and used linear discriminant analysis and step-wise selection to select the best subset of features. Gibbs et al.[40] applied texture analysis based on Haralick features and used logistic regression analysis with backwards elimination method to select the most discriminating subset of texture features. Gal et al.[41] compared different classifiers (logistic regression, linear discriminant analysis, bayesian and support vector machine) combining kinetic and morphological features, and using an exhaustive search to select the best features.

In the following a multiparametric model is presented, which combines a selection of morphological and kinetic features for discriminating malignant from benign mass-like breast lesions at DCE-MRI[42]. Original features are introduced and combined with features already presented in literature, with the aim of trying a different approach. Model selection is performed by a genetic search[43] and a wrapper approach[44] using a support vector regressor.

1.4.1 Method

To validate the method, 73 mass-like lesions were retrospectively used. Lesions were detected in 51 exams acquired at two centers at 1.5 T with MRI protocols described in 1.2.2 and confirmed by histopathology (54 malignant and 19 benign). Lesions were automatically segmented after image normalization and elastic registration of contrast-enhanced frames, as described in the previous steps, and then selected by two experienced radiologists in order to exclude non mass-like lesions or blood vessels.

Lesion size was 13±8.4 mm (mean±standard deviation) for benign lesions and 16.1±14.7 mm) for malignant lesions, with lesion size determined as the longest diameter measured by radiologists. 33 lesions had a size smaller than 10 mm (22 malignant, 11 benign), whereas 40 lesions had a size larger than 10 mm (32 malignant, 8 benign). Table x.3 summaries lesions histology.

Table x.3 histological types of the 73 lesions included in the study

Tumor types	Number
Malignant lesions	54
Invasive ductal carcinoma (IDC)	36
Invasive lobular carcinoma(ILC)	4
Ductal carcinoma in-situ (DCIS)	4
Mixed Invasive Carcinoma	10
Benign lesions	19
Fibroadenoma (FAD)	9
Papilloma	4
Other benign lesions	6

For each lesion, a set of 19 features were automatically extracted: 10 morphological features, related to shape, margins, and internal contrast-enhancement distribution, and 9 kinetic features computed from signal-to-time intensity curves.

Two morphological features related to the lesion shape are calculated on the binary mask: circularity[38] and convex index[45].

Three features are used to describe the margin of a lesion: irregularity[38], mean and standard deviation of angles between surface normals ((mean(ABSN), std(ABSN))[46].

Other five features characterizing the internal enhancement pattern are extracted: the autocorrelation function (evaluated at 2mm displacement), two

features related to the peripheral uptake and the mean and standard deviation of the shape index(SI)[47] computed inside the segmented mass.

Enhancement kinetics features are used to characterize the time course of signal intensity through the contrast enhancement defined as:

$$C(\mathbf{r},j) = \frac{S(\mathbf{r},j) - S(\mathbf{r},0)}{S(\mathbf{r},0)} \qquad j = 1,\ldots,N \ (N = 5/6) \tag{x.3}$$

where S(**r**,i) is the intensity at voxel location *r* at time frame *i* and it is normalized to the contrast enhancement of mammary vessels. Two types of features are derived from the contrast enhancement. The first type is related to the fitting of the contrast enhancement to the following analytical exponential function:

$$C(t) = Ate^{-t^D} \tag{x.4}$$

where the coefficients *A* and *D* control the function amplitude and decay, respectively. These coefficients characterize therefore the contrast uptake and washout inside the lesion. The lesion uptake and washout of contrast material were characterized by fitting the contrast enhancement C(**r**,i) with an analytical function rather than using a two-compartmental pharmaco-kinetic model[48]. The use of a pharmaco-kinetic model implies strict constrains in the acquisition protocols[49], that were not fulfilled in the acquisition of many clinical datasets. Although, the analytical function proposed (Eqn. x.4) cannot model physiologically the lesion, its simple form allows for relaxing constrains on the acquisition protocols still characterizing the kinetic behaviour of the lesion.

The second type of feature computes the area under the contrast enhancement curve C(**r**,t), AUCEC. This feature is related to the total amount of contrast material in the lesion tissue. The mean, standard deviation and entropy were computed in the lesion segmented volume, yielding a total of 9 contrast enhancement kinetic features.

A support vector machine (SVM) was trained with feature subsets selected by a genetic search. Best subsets were composed of the most frequent features selected by majority rule. The performance was measured by receiver operator characteristics (ROC) analysis with the 10-fold cross-validation method that prevents optimistically biased evaluations due to overfitting. The bootstrap technique was used in order to estimate the confidence interval of area under ROC (AUC) and to compare the classification performances of the different features subsets. A Wilcoxon matched pairs one-tailed test was also performed to determine the significance level of the performance improvement.

1.4.2 Results

Figure x.9 shows the mean ROC curves related to the feature subsets selected in separated genetic searches for each class of features and to the features subset selected by the genetic search using both classes of features.

The AUC obtained in the three genetic searches were 0.90±0.06 (mean±standard deviation) for the morphological features subset, 0.87±0.06 for the kinetic features subset, and 0.94±0.03 with the combined feature subset. The AUC resulted from the combined feature subset was significantly higher (p-value < 0.01) than those obtained with the other feature subsets, showing that the combination of features increases the classification performances.

Three morphological features (mean(ABSN), std(ABSN), peripheralUptake) and three kinetic features (mean(D), entropy(D), entropy(A)) were selected in separated genetic searches for each feature class. Four features (mean(ABSN), std(SI), mean(D), mean(AUCEC)) were selected from the combined use all two classes of features.

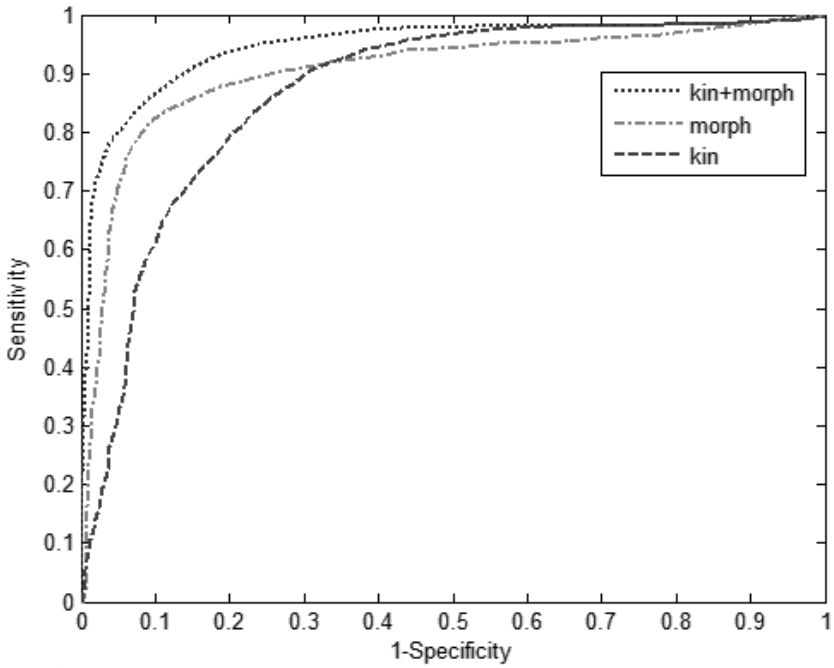

Figure 2 ROC curves associated to the feature subsets selected in separated genetic searches for each class of features and to the features subset selected by the genetic search using all two classes of features.6

1.5 Discussion and Conclusions

The CAD system here presented (CADBREAST MRI, research version, im3D) achieves good performance in detecting and discriminating breast lesions in a fully automatic way, thus having the potential of reducing inter- and intra-observer variability and reading time[19,21].

The lesion detection step achieved a sensitivity of 98%, with an acceptable number of FP findings. Moreover, the good performances obtained in detecting satellite lesions (16 of 17 were identified) highlights the system's potential in helping the detection of multifocal and multicentric breast cancers.

The widespread use of the DCE-MRI in the clinical practice is slowed down by the lack of automatic methods able to make its analysis less time consuming and independent on the expertise of the radiologist. Few methods have been developed to detect and characterize breast lesions automatically with DCE-MRI. Ertas et al. developed an automatic algorithm for the detection of breast lesions based on cellular neural network segmentation and 3D template matching[22], but their dataset was composed only by non-fat-sat images and they applied a fixed threshold to extract suspicious areas, limiting the applicability to studies acquired with different protocols. They assessed the performance of the system on a dataset of 39 lesions (19 benign and 20 malignant), obtaining a detection rate of 100% with less than one FP per study. An automatic lesion detection method based on support vector machine, proposed by Twellmann et al. also showed promising results, yielding an area under the ROC curve of 0.98. However, the algorithm was tested on a limited dataset of 12 patients and only on non-fat-sat images[24].

The innovation of the proposed lesion detection method relies on the possibility to be used with both fat-sat and non-fat-sat images, since the normalization is not performed by dividing each enhanced images by the unenhanced one, but using an intrinsic value of the image related to contrast agent administration. The normalization process used in literature, in fact, yields very noisy images if fat-sat is applied, as most of the breast signal is suppressed in the unenhanced frame. On the other hand the proposed normalization requires that the mammary vessels are included in the field of view with an adequate spatial resolutions, therefore the DCE-MRI should be performed on the axial plane.

A second innovation relies on the use of the mIPT instead of the commonly used MIPT (maximum intensity projection over time). The MIPT is very sensitive to artifacts and noise and, due to the the ''blooming sign'' effect[50–52], the lesion size could be overestimated. Vice versa, the use of the mIPT may produce an underestimation of the lesion size by averaging over time, but allows more reliable segmentations being less sensitive to noise, thus having a lower number of FPs.

The higher number of FPs compared to other commercial and academic software[53] is a limitation of the proposed method. As most of the FPs are vessels, mainly tortuous vessels or bifurcations with low vesselness values[54,55], a step of fully automatic blood vessels detection is ongoing, aiming to dramatically decrease the number of FPs. Moreover, improving the accuracy of the breasts segmentation step, especially around the ribcage area, could lead to increase the specificity of the lesion detection step.

In the proposed method the lesion detected were analyzed and discriminated by a classifier based on the support vector machine. For this step a more accurate identification of lesion boundary and morphology could be useful, and a further refinement of the lesion segmentation may become necessary, even if the results obtained during the lesion discrimination step are satisfactory.

The classifier here proposed is able to discriminate malignant from benign breast mass-like lesions using two groups of features (morphological and kinetic), and obtaining a AUC of 0.94±0.03. The AUC for the feature selection (FS) resulting from the combination of all two feature groups was significantly higher than those obtained with all other selected FSs, showing that the combination of features increases the classification performances.

A genetic algorithm was used to select feature subsets, in order to prevent unnecessary computation, overfitting, and to ensure a reliable classifier. The main limitation of the discrimination step is the limited number of lesions. This can produce overfitting of the training data, leading to overestimate the classifier's performance. In order to reduce these effects, the total number of features was limited to 19 and the selected feature subsets were composed only of 3 to 4 features. Moreover, classification performances were evaluated with a stratified 10-fold cross-validation method to reduce the classification bias.

Another limitation is the unbalanced dataset. The number of malignant lesions is higher than benign lesions, leading to a possible bias in the discrimination of malignancy. This problem was partially reduced by presenting at training the same number of malignant and benign lesions using copies of benign lesions. Nevertheless, the benign class can be poorly described in the feature space.

In conclusion, the proposed CAD system was tested on MR datasets obtained from different scanners, with a variable temporal and spatial resolution and on both fat-sat and non fat-sat images, and has shown promising results. This type of system could potentially be used for early diagnosis and staging of breast cancer to reduce reading time and to improve detection, especially of the smaller satellite nodules. Further refinements are ongoing to improve vessel detection, breast segmentation and to validated these conclusions on a larger dataset.

References

1. M. C. Mahoney, T. Bevers, E. Linos, W. C. Willett, "Opportunities and strategies for breast cancer prevention through risk reduction". *CA Cancer J. Clin.* **58,** 347–371 (2008).
2. P. Boyle, J. Ferlay, "Cancer incidence and mortality in Europe, 2004", *Ann. Oncol.* **16,** 481–488 (2005).
3. Q. Wu, M. K. Markey, "Computer-Aided Diagnosis of Breast Cancer on MR Imaging", *Recent Advances in Breast Imaging, Mammography, and Computer-Aided Diagnosis of Breast Cancer,* J. S. Suri, R. M. Rangayyan, Ed., chapter 22, SPIE The International Society for Optical Engineering, Bellingham, WA (2006).
4. K. Chakraborti, P. Bahl, M. Sahoo, S. Ganguly, C. Oberoi, "Magnetic resonance imaging of breast masses: comparison with mammography", *Indian J. Radiol. Imaging* **15,** 381–387 (2005).
5. F. Montemurro, L. Martincich, I. Sarotto, et al., "Relationship between DCE-MRI morphological and functional features and histopathological characteristics of breast cancer", *Eur. Radiol.* **17**, 1490–1497 (2007).
6. C. K. Kuhl, "The current status of breast MR imaging. Part I. Choice of technique, image interpretation, diagnostic accuracy, and transfer to clinical practice"*, Radiology* **244,** 356–378 (2007).
7. C. K. Kuhl, "Current status of breast MR imaging. Part 2. Clinical applications", *Radiology* **244,** 672–691 (2007).
8. F. Sardanelli, G. M. Giuseppetti, G. Canavese, et al., "Indications for breast magnetic resonance imaging. Consensus document, ''Attualita in senologia'', Florence 2007". *Radiol. Med.* **113,** 1085–1095 (2008).
9. F. Sardanelli, C. Boetes, B. Borisch, et al., "Magnetic resonance imaging of the breast: recommendations from the EUSOMA working group", *Eur. J. Cancer* **46**, 1296–1316 (2010).
10. L. C. Wang, W. B. De Martini, S. C. Partridge, S. Peacock, C. D. Lehman, "MRI-Detected Suspicious Breast Lesions: Predictive Values of Kinetic Features Measured by Computer-Aided Evaluation", *A. J. R.* **193**(3), 826-831 (2009).
11. D. Rueckert, L. I. Sonoda, C. Hayes, D. L. Hill, M. O. Leach, D. J. Hawkes, "Nonrigid registration using free-form deformations: application to breast MR images", *IEEE Trans Med Imaging* **18,** 712–721 (1999).
12. L. Ibàñez, Schroeder W. Ng Lydia et al., *The ITK Software Guide,* First Edition, Kitware Inc. (2005)
13. D. Mattes, D. Haynor, H. Vesselle, T. W. E. Lewellyn, "Nonrigid multimodality image registration", *Proceedings of the Medical Imaging*

Conference of SPIE, International Society for Optical Engineering, Volume **4322**, 1609–1620, San Diego, CA (2004).

14. C. Broyden, "The convergence of a class of double-rank minimization algorithms 1. General considerations", *IMA J. Appl. Math.* **6**, 76–90 (1970).
15. L. A. Carbonaro, D. Persano, S. Delsanto, D. Brizzi, A. Vignati, V. Giannini, L. Morra, A. Bert, F. Sardanelli, "Non-rigid registration of contrast-enhanced (CE) MR images of the breast", *Proc. European Congress of Radiology*, 4-8 March 2010, Vienna, Austria.
16. L. Carbonaro, D. Persano, S. Delsanto, D. Brizzi, A. Vignati, V. Giannini, A. Bert, F. Sardanelli, "Evaluation of non-rigid registration method for MR with contrast agent injection images applied to the breast", *Proc. National Conference of Senology*, Ancona, 18-20 June 2009.
17. J.D. Gibbons, Nonparametric Statistical Inference, 2nd Ed.,M. Dekker, (1985).
18. I. Bankman, T. Nizialek, I. Simon, O. Gatewood, I. Weinberg, W. Brody, "Algorithms for segmenting small-low contrast objects in images", *Recent Advances in Breast Imaging, Mammography, and Computer-Aided Diagnosis of Breast Cancer,* J. S. Suri, R. M. Rangayyan, Ed., chapter 21, SPIE The International Society for Optical Engineering, Bellingham, WA (2006).
19. S. Mussurakis, D. L. Buckley, A. Horsman, "Dynamic MRI of invasive breast cancer: assessment of three region-of-interest analysis methods", *J. Comput. Assist. Tomogr.* **21**, 431–438 (1997).
20. G. P. Liney, P. Gibbs, C. Hayes, M. O. Leach, L. W. Turnbull, "Dynamic contrast-enhanced MRI in the differentiation of breast tumors: user-defined versus semi-automated region-of-interest analysis", *J. Magn. Reson. Imaging* **10**, 945–949 (1999).
21. T. Niemeyer, C. Wood, K. Stegbauer, J. Smith, "Comparison of automatic time curve selection methods for breast MR CAD", *Proceedings of the Medical Imaging Conference of SPIE*, International Society for Optical Engineering, Volume **5370**, 785–790, San Diego, CA (2004).
22. G. Ertas, H. O. Gulcur, O. Osman, O. N. Ucan, M. Tunaci, M. Dursun, "Breast MR segmentation and lesion detection with cellular neural networks and 3D template matching", *Comput. Biol. Med.* **38**,116–126 (2008).
23. B. J. Woods, B. D. Clymer, T. Kurc, et al., "Malignant-lesion segmentation using 4D co-occurrence texture analysis applied to dynamic contrast-enhanced magnetic resonance breast image data", *J. Magn. Res. Im.* **25**, 495–501 (2007).
24. T. Twellmann, A. Saalbach, C. Muller, T. W. Nattkemper, A. Wismuller, "Detection of suspicious lesions in dynamic contrast enhanced MRI data", *Proc IEEE Eng Med Biol Soc* **1**, 454–457 (2004).

25. R. M. Mann, C. K. Kuhl, K. Kinkel, C. Boetes, "Breast MRI: guidelines from the European Society of Breast Imaging", Eur. Radiol. **18**, 1307–1318 (2008).

26. A. Vignati, V. Giannini, M. De Luca et al. "Performance of a fully automatic lesion detection system for breast DCE-MRI", accepted for publication by *J. Magn. Res. Im. (2011)*.

27. N. Otsu, "A threshold selection method from gray-level histograms", *IEEE Trans Syst Man Cybern B Cybern* **9**, 62–66 (1979).

28. I. Gribbestad, K. Gjesdal, G. Nilsen, S. Lundgren, M. Hjelstuen, A. Jackson, "An introduction to dynamic contrast-enhanced MRI in oncology", *Dynamic contrast-enhanced magnetic resonance imaging in oncology*, A. Jackson, D. Buckley, G. J. M. Parker, Ed., p 3–20, Springer Verlag, Heidelberg (2005).

29. S. H. Heywang-Kobrunner, R. Beck, *Contrast-enhanced MRI of the breast,* pp. 229, Springer, New York (1996).

30. L. A. Carbonaro, N. Verardi, G. Di Leo, F. Sardanelli, "Handling a high relaxivity contrast material for dynamic breast MR imaging using higher thresholds for the initial enhancement", *Invest. Radiol.* **45**, 114–120 (2010).

31. F. Sardanelli, A. Fausto, A. Esseridou, G. Di Leo, M. A. Kirchin, "Gadobenate dimeglumine as a contrast agent for dynamic breast magnetic resonance imaging: effect of higher initial enhancement thresholds on diagnostic performance", *Invest. Radiol.* **43**, 236–242 (2008).

32. F. Sardanelli, A. Iozzelli, A. Fausto, A. Carriero, M. A. Kirchin, "Gadobenate dimeglumine-enhanced MR Imaging breast vascular maps: association between invasive cancer and ipsilateral increased vascularity", *Radiology* **235**, 791–797 (2005).

33. L. Antiga, "Generalizing vesselness with respect to dimensionality and shape", *The Insight Journal* - 2007 July - December. Available at: http://hdl.handle.net/1926/576. Accessed September 2011.

34. Y. Sato, S. Nakajima, N. Shiraga, et al., "Three-dimensional multi scale line filter for segmentation and visualization of curvilinear structures in medical images", *Med. Image Anal.* **2**, 143–168 (1998).

35. ACR Practice guideline for the performance of contrast-enhanced magnetic resonance imaging (MRI) of the breast. 2008. Available at: http://www.acr.org/secondarymainmenucategories/quality_safety/guidelines/breast/mri_breast.aspx. Accessed September 2011.

36. C. K. Kuhl, P. Mielcareck, S. Klaschik, et al., "Dynamic breast MR imaging: are signal intensity time course data useful for differential diagnosis of enhancing lesions?" *Radiology* **211**, 101–110, (1999).

37. Breast imaging reporting and data system (BIRADS). 2003. Available at: http://www.acr.org/SecondaryMainMenuCategories/quality_safety/BIRADS

Atlas/BIRADSAtlasexcerptedtext/BIRADSMRIFirstEdition.aspx Accessed September 2011.

38. K. G. Gilhuijs, M. L. Giger, U. Bick. "Computerized analysis of breast lesions in three dimensions using dynamic magnetic-resonance imaging" *Med. Phys*. **9**, 1647–1654 (1998).
39. K. G. Gilhuijs, E. Deurloo, et al., "Breast MR imaging in women at increased lifetime risk of breast cancer: clinical system for computerized assessment of breast lesions", *Radiology* **225,** 907-916 (2002).
40. P. Gibbs, L. Turnbull, "Textural analysis of contrast-enhanced images of the breast", *Magn. Reson. Med.* **50**, 92-98 (2003).
41. Y. Gal, A. Mehnert, A. Bradley et al., "Feature and Classifier Selection for Automatic Classification of Lesions in Dynamic Contrast-Enhanced MRI of the breast", *Proceedings Digital Image Computing: Techniques and Applications (DICTA)*,132-139 (2009).
42. S. Agliozzo, M. De Luca L. Martincich et al., "A Multiparametric Model Combining a Selection of Morphological, Kinetic, and Spatio-temporal Features of Mass-like Lesions at Breast MRI" Proceedings of RSNA Annual Meeting, November 28- December 3, Chicago IL (2010). Available at: http://rsna2010.rsna.org/search/search.cfm?action=add&filter=Author&value=89595
43. L. J. Eshelman, *The CHC adaptive search algorithm*, Foundations of genetic Algorithms, Ed San Mateo, CA (1991) .
44. R. Kohavi and G. John, "Wrappers for feature subset selection", Artif. Intell. **97,** 273-324 (1997)
45. C. B. Barber, D. P. Dobkin, H. T. Huhdanpaa, "The Quickhull Algorithm for Convex Hulls," ACM Trans. Math. Software **22,** 469-483 (1996).
46. T. Zhang, G. Nagy, "Surface turtuosity and its application to analyzing cracks in concrete", *Proceeding of the IAPR International Conference on Pattern recognition*, 851-854 (2004).
47. J. Koenderink, *Solid Shape*, MIT Press, Cambridge, MA, (1990).
48. P. Tofts "Modelling Tracer Kinetics in Dynamic Gd-DTPA MR Imaging" J. Magn. Res. Imag **7**, 91-101 (1997).
49. E. Henderson, B.K. Rutt, T.Y. Lee, "Temporal sampling requirements for the tracer kinetics modeling of breast disease", Magn. Reson. Imaging **16** 1057-1073 (1998).
50. Dietzel M, Baltzer PA, Vag T, et al. Differential Diagnosis of Breast Lesions 5 mm or Less: Is There a Role for Magnetic Resonance Imaging? J Comput Assist Tomogr 2010;34(3):456-464.

51. Penn A, Thompson S, Brem R, et al. Morphologic blooming in breast MRI as a characterization of margin for discriminating benign from malignant lesions. Acad Radiol 2006;13(11):1344-1354.
52. Fischer DR, Wurdinger S, Boettcher J, Malich A, Kaiser WA. Further signs in the evaluation of magnetic resonance mammography - A retrospective study. Invest Radiol 2005;40(7):430-435.
53. Kurz KD, Steirthaus D, Klar V, et al. Assessment of three different software systems in the evaluation of dynamic MRI of the breast. Eur J Radiol 2009;69(2):300-307.
54. Kirbas C, Quek F. A review of vessel extraction techniques and algorithms. Acm Comput Surv 2004;36(2):81-121.
55. Freiman M, Joskowicz L, Sosna J. A variational method for vessels segmentation: algorithm and application to liver vessels visualization. Proceedings of the Medical Imaging Conference of SPIE. Volume 7261. Orlando, FL: International Society for Optical Engineering; 2009. p. 72610H-72610H-72618